



# Robust Cardiac Feature Monitoring based on Millimeter-Wave Radar

Thesis submitted in accordance with the requirements of the University of Liverpool  
for the degree of Doctor in Philosophy by

**Yuanyuan Zhang**

May 2025



# **Abstract**

Paraphrasing the Code of Practice: each copy of the thesis must contain an abstract indicating the aims of the investigation and the results achieved. It should be no longer than one side of an A4 sheet (normally about 450 words).



# Acknowledgements

I would like to thank people.



# Publications

## Journal paper:

1. **Yuanyuan Zhang**, Runwei Guan, Lingxiao Li, Rui Yang, Yutao Yue, Eng Gee Lim, “radarODE: An ODE-Embedded Deep Learning Model for Contactless ECG Reconstruction from Millimeter-Wave Radar”, *IEEE Transactions on Mobile Computing*, Apr. 2025.
2. **Yuanyuan Zhang**, Rui Yang, Yutao Yue, Eng Gee Lim, “radarODE-MTL: A Multi-Task Learning Framework with Eccentric Gradient Alignment for Robust Radar-Based ECG Reconstruction”, *IEEE Transactions on Instrumentation and Measurement*, Apr. 2025.
3. **Yuanyuan Zhang**, Rui Yang, Yutao Yue, Eng Gee Lim, Zidong Wang, “An Overview of Algorithms for Contactless Cardiac Feature Extraction From Radar Signals: Advances and Challenges”, *IEEE Transactions on Instrumentation and Measurement*, Jul. 2023.

## Conference paper:

1. **Yuanyuan Zhang**, Sijie Xiong, Rui Yang, Eng Gee Lim, Yutao Yue, “Recover from Horcrux: A Spectrogram Augmentation Method for Cardiac Feature Monitoring from Radar Signal Components”, in *2025 47th Annual International Conference of the IEEE Engineering in Medicine & Biology Society (EMBC2025)*, IEEE, Jul. 2025.

## Under Review:

1. **Yuanyuan Zhang**, Haocheng Zhao, Sijie Xiong, Rui Yang, Eng Gee Lim, Yutao Yue, “From High-SNR Radar Signal to ECG: A Transfer Learning Model with Cardio-Focusing Algorithm for Scenarios with Limited Data”, *IEEE Transactions on Mobile Computing*. (Under Review)
2. Sijie Xiong, **Yuanyuan Zhang**, Cheng Tang, Haoling Xiong, Yiding Li, Atsushi Shimada, “U-MA: A Unified Framework with Differential Mamba under Parallel U-Net Scheme for Time Series Forecasting”, *Engineering Applications of Artificial Intelligence*. (Under Review)
3. Sijie Xiong, Cheng Tang, **Yuanyuan Zhang**, Haoling Xiong, Youhao Xu, Atsushi Shimada, “CME-Mamba with Enhancing Nonlinear Dependencies for Time Series Forecasting”, *Applied Soft Computing*. (Under Review)

# Contents

<b>Abstract</b>	i
<b>Acknowledgements</b>	iii
<b>Publications</b>	v
<b>Contents</b>	viii
<b>List of Figures</b>	x
<b>List of Tables</b>	xi
<b>List of Acronyms</b>	xii
<b>1 Introduction</b>	1
1.1 Wireless Sensing for Vital Sign Monitoring . . . . .	1
1.2 Radar-based Vital Sign Monitoring . . . . .	2
1.3 Challenges in Radar-based ECG Recovery . . . . .	5
1.4 Contributions and Thesis Outline . . . . .	8

<b>2 Background and Literature Review</b>	<b>11</b>
2.1 Background for Radar-based Cardiac Monitoring . . . . .	11
2.2 Literature Review . . . . .	11
<b>3 High-SNR Radar Signal</b>	<b>12</b>
3.1 Introduction . . . . .	12
3.2 Theoretical Background and Challenges . . . . .	15
3.3 Methodology . . . . .	18
3.4 Details of Experiment and Dataset . . . . .	27
3.5 Experimental Results and Evaluations . . . . .	30
3.6 Conclusions . . . . .	38
<b>4 Chapter</b>	<b>39</b>
<b>5 Chapter</b>	<b>40</b>
<b>6 Chapter</b>	<b>41</b>
<b>7 Chapter</b>	<b>42</b>
<b>References</b>	<b>43</b>

# List of Figures

1.1	Illustration of different steps in radar-based cardiac monitoring. . . . .	3
1.2	Overview of the thesis with unsolved challenges. . . . .	8
3.1	Challenges for radar-based ECG recovery: (a) and (b) Radar signals with high and low SNR for adjacent points with a distance of 0.03m; (c) and (d) Inference results of a well-trained deep learning model in original and new scenarios. . . . .	17
3.2	Overview of the CFT-RFcardi framework: (a) Rough localization of human body; (b) Use CFT to find CF point and extract high-SNR radar signals; (c) Transfer learning with pre-text task training and fine-tuning stages. . . . .	19
3.3	Procedures for obtaining RA map: (a) Range FFT for chirps along fast time; (b) Angle FFT along virtual channels. . . . .	20
3.4	Template for assessing SNR: (a) High-SNR radar signal; (b) Extracted signal envelope with the synthetic template; (c) (a) Low-SNR radar signal, (d) Extracted signal envelope with the synthetic template. . .	22

3.5	Illustration of the CFT algorithm with bold line wrapping the search region $S_k$ : (a) Equality between $\gamma$ and $\Gamma$ (same as in CS algorithm); (b) Large $\Gamma_k$ with refined $\gamma_k$ , providing more potential points to be evaluated; (c) Jump out of the local minimum by adjusting $\Gamma_k$ and $\gamma_k$ .	23
3.6	Indoor scenarios for data collection.	27
3.7	Visualization of the extracted radar signal for all methods: (a) - (c) If CF point is around rough body location; (d) - (f) If CF point is far from rough body location.	29
3.8	Illustration of performance in terms of peak error and MDR: (a) - (b) Scattered points with fitting curves along range axis; (c) - (d) CDF plots for all trials.	32
3.9	Impact of radar input quality on the final ECG recovery: (a) - (b) High-quality radar input and ECG recovery; (c) - (d) Low-quality radar input and ECG recovery.	34
3.10	Results of SSR: (a) Failed SSR due to lack of data and sparse penalty; (b) Ideal SSR result with good MSE and sparsity.	35
3.11	Results of transfer learning using limited labeled data: (a) Poor ECG recovery without proper morphological feature and peak location; (b) Good ECG recovery owing to the pre-trained model.	37
3.12	Overall performance of the radar-based ECG recovery.	38

# List of Tables

3.1	Parameters for data collection interface . . . . .	28
3.2	Performance of supervised ECG recovery . . . . .	33
3.3	Performance of SSL with ablation study . . . . .	33
3.4	Performance of ECG Recovery using different percentages of labeled data	37

# Acronyms

<b>CF</b>	cardio-focused
<b>CFT</b>	cardio-focusing and -tracking
<b>DFO</b>	derivative-free optimization
<b>DNN</b>	deep neural network
<b>ECG</b>	electrocardiogram
<b>EGA</b>	eccentric gradient alignment
<b>FMCW</b>	frequency modulated continuous wave
<b>HR</b>	heart rate
<b>HRV</b>	heart rate variability
<b>IQ</b>	in-phase and quadrature
<b>mmWave</b>	millimeter wave
<b>MTL</b>	multi-task learning
<b>PPI</b>	peak-to-peak interval
<b>RBM</b>	random body movement
<b>Rxs</b>	receivers
<b>SCEG</b>	single-cycle ECG generator

**SCG** seismocardiography

**SNR** signal-to-noise ratio

**SSL** self-supervised learning

**Txs** transmitters



# Chapter 1

## Introduction

The World Health Organization highlights that the worldwide population is aging rapidly, with one in six people globally being over 60 by 2030, and the number of elderly people over 60 will double to 2.1 billion by 2050. This demographic shift brings significant challenges, including a higher prevalence of chronic diseases, frailty, and complex health conditions among older adults. Maintaining health and independence in later life is crucial not just for individuals, but for families and societies [1]. As the world population ages, the early detection of diseases and daily monitoring of health conditions become critical to reducing the need for institutional care and improving quality of life, but reaching assistance from professional caregivers might be expensive or inconvenient especially when most of the older population will live in low- and middle-income countries [1]. Therefore, the current labor-intensive wellness monitoring needs a revolution, and wireless vital sign monitoring addresses these challenges by enabling continuous, automated monitoring of health indicators or emergency events (e.g., heart rate and fall detection) without constant human intervention.

### 1.1 Wireless Sensing for Vital Sign Monitoring

In the recent decade, wireless sensing has emerged as a transformative paradigm that leverages electromagnetic waves to remotely detect changes and gather information

about objects, environments, and biological entities, and this non-invasive approach has been embedded in a wide range of applications from healthcare monitoring to autonomous driving, leading the rapid evolution of information and communication technologies towards the next generation [2–4]. Different from traditional contact-based sensing methods that require physical connections to the subject or environment, wireless sensing can be seamlessly integrated into daily life, fostering innovation in smart infrastructure and personalized health systems. For example, By leveraging radio frequency signals to detect subtle physiological movements such as respiration and heartbeat, radar-based systems eliminate the need for physical contact while maintaining clinical-grade accuracy, addressing key limitations of traditional wired sensors that cause patient discomfort, skin irritation, and infection risks.

Various wireless sensors can be utilized for vital sign monitoring according to the information received. For example, optical or thermal cameras sense the skin colour or temperature variation caused by heartbeats [5, 6], acoustic sensors can monitor the heart sound [7], and Wi-Fi routers extract cardiac features from the channel state information [8]. However, the aforementioned sensors may be blamed for privacy issue [9], low accuracy [10] or vulnerability to the changing environment (e.g., light conditions or temperature variations) [11]. In contrast, radar senses the ambient environment through reflected signals mixed by chest wall displacement (induced by respiratory and cardiac activities) and all kinds of ambient noises [12], requiring proper algorithms to further extract the latent vital features. Additionally, compared with cameras, Wi-Fi routers and acoustic sensors, radar signal propagation is neither vulnerable to the illumination/temperature/sound variations nor privacy-intrusive. Therefore, radar-based vital sign monitoring is promising to realize unobtrusive sensing in most scenarios after the design of advanced signal-processing algorithms.

## 1.2 Radar-based Vital Sign Monitoring

The first attempt at radar-based vital sign monitoring can be traced back to 1975 by measuring the displacement of the chest wall induced by respiration [13]. The chest wall displacement will modulate the phase component of the emitted radar signal, and

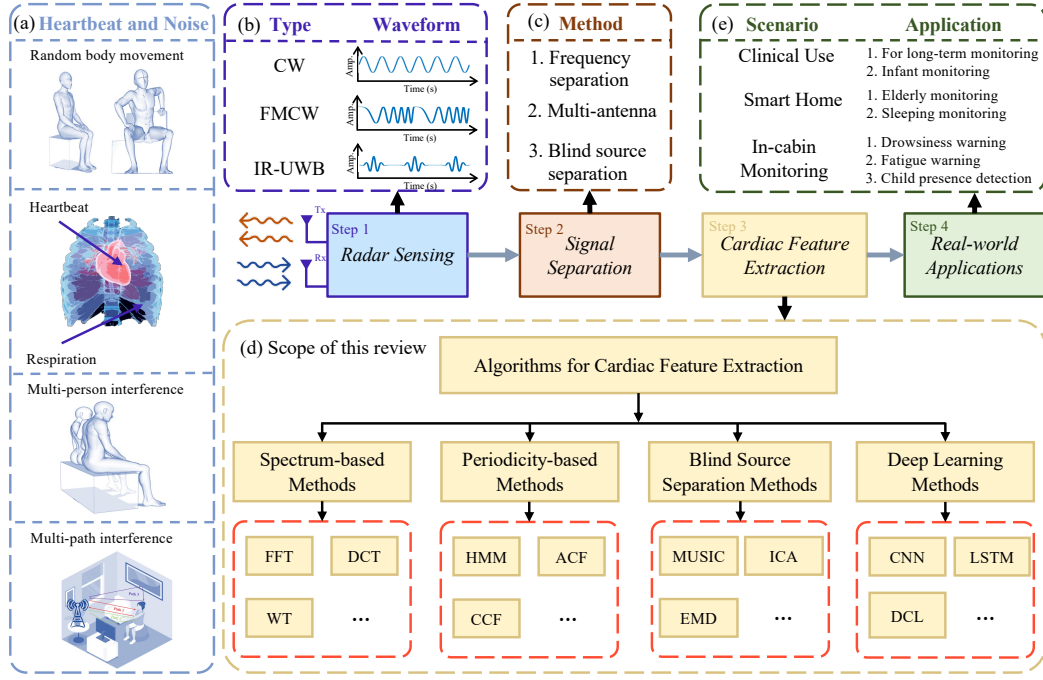


Figure 1.1: Illustration of different steps in radar-based cardiac monitoring.

the latent respiratory information can be demodulated from the phase variation [12]. Similarly, cardiac activities are small-scale displacements that also cause chest wall displacements, but such small displacements are normally ruined by respiration with orders more amplitude.

The overview of the radar-based cardiac monitoring process and the downstream applications are shown in Figure 1.1. To measure the target cardiac features, the first step is to transmit the radio frequency signals with certain waveforms to sense the ambient environment as illustrated in Figure 1.1(b). After reflection, the received signals contain not only the target signal (vibration caused by heartbeats) but also other noise signals such as random body movement (RBM), respiration and multi-person or multi-path interferences, as shown in Figure 1.1(a). The second step aims to isolate the signal reflected by a single human body from the background clutter or the interference from neighbours using specific methods, as shown in Figure 1.1(c) [14]. The third step is to extract the cardiac features from the reflected signals of a single

person using various algorithms, with detailed classification provided in Figure 1.1(d). The last step is to analyse the obtained cardiac features for specific downstream applications as shown in Figure 1.1(e).

Most early studies focused on the recovery of coarse cardiac information, such as heart rate (HR), heart sound and heart rate variability (HRV), from the perspectives of radar front-end design or advanced algorithms design [2]. For example, some advanced types of radar (e.g., frequency modulated continuous wave (FMCW) radar) are designed to enable high range-resolution or multi-person monitoring [15], and some baseband signal-processing algorithms are embedded on the radar platform to realize in-phase and quadrature (IQ) modulation or accurate phase unwrapping [16]. In addition, various advanced algorithms are applied by leveraging different intrinsic characteristics of cardiac activities to robustly reconstruct cardiac features. For example, cardiac activities normally reveal strong periodicity in the time domain and have dominant peaks on the spectrum, inspiring periodicity-based methods (e.g., template matching [17], hidden Markov model [11]) and spectrum-based methods (e.g., Fourier transform [18], wavelet transform [19]) as two major categories in cardiac feature extraction algorithms.

In recent years, the emergence of commercial radar platforms with high operating frequency (i.e., millimeter wave (mmWave) radar) encourages researchers to extract fine-grained cardiac features (e.g., electrocardiogram (ECG) and seismocardiography (SCG)) from the radar signal [2]. SCG signal is measured by the accelerometer mounted on the human chest to measure the mechanical vibrations produced by heartbeats, describing the fine-grained cardiac mechanical activities such as aortic/mitral valve opening/closing and isovolumetric contraction [20]. Although these vibrations are subtle, it is still reasonable to directly map the displacements detected by radar to each fine-grained cardiac mechanical activity using high-resolution radar as proved in [15]. However, the SCG measurement is not widely used in clinical scenarios, while the ECG signal is commonly recognized as the golden standard in cardiac monitoring because ECG describes the fine-grained cardiac activities, such as atrial/ventricular depolarization/repolarization, through the featured waveform (i.e., PQRST peaks) and is crucial to the diagnosis of cardiovascular diseases [21].

Based on the discussions above, it is believed that radar-based ECG recovery is an essential research direction to enable the realization of future wellness monitoring, even providing fine-grained cardiac features for clinical diagnosis. This thesis will thoroughly investigate all the stages in radar-based ECG recovery with multiply inventions proposed to overcome the unsolved challenges.

## 1.3 Challenges in Radar-based ECG Recovery

The realization of radar-based ECG recovery needs two general stages: (a) radar signal collection and pre-processing to increase signal-to-noise ratio (SNR); (b) ECG recovery from radar signal to realize domain transformation from cardiac mechanical activities to electrical activities using deep neural network (DNN), and this thesis will elaborate on four challenges figured in both stages with corresponding solutions proposed.

### 1.3.1 The First Challenge

In the literature, many studies are dedicated to inventing advanced signal processing algorithms to enhance the signal quality, because the deep learning model for ECG recovery is vulnerable to the inputs contaminated by noises and requires high-SNR radar signals as inputs [22, 23]. The methods for capturing high-SNR radar signals can be categorized into two groups:

- The first type of method focuses on designing advanced radar front-end with multiple transmitters (Txs) and receivers (Rxs) [24, 25] or calibrating baseband radar signals from in-phase and quadrature (IQ) channels to a circular shape [26–28].
- The second type of method assumes that the rough localization of human body provides accurate chest region with the majority of range bins containing useful cardiac features, and high-SNR signal can be obtained by selecting useful

channels [29,30], applying clustering algorithms [22] or accumulating the signals from various dimensions (e.g., chirps, frames, antennas) [23].

The first type of method is not suitable for some commonly used frequency-modulated continuous-wave (FMCW) radar platforms (e.g., TI AWR-x radar) due to the on-board digital front-end module filtering the frequency-modulated feature of baseband signal (i.e., circular IQ plot) [31], preventing the broad applications of this approach in commercial radar. The second type of method relies on accurate localization of the chest region, while the existing methods only provide a rough location of the human body, causing a deviation of several decimeters due to different postures of the subject [32]. Therefore, the methods based on signal accumulation may fail because only a minority of range bins contain cardiac features, hence not subjecting to the law of large numbers [23]. Although some aforementioned studies have proposed methods for selecting or clustering the useful range bins with cardiac features [22,29], the computational cost for traversing a large objective space can be huge without an accurate cardiac location. In this case, the **first challenge** is to precisely locate and track the cardiac location during data collection to efficiently extract high-SNR radar signal.

### 1.3.2 The Second Challenge

To reconstruct ECG from radar signal, the researchers must deal with domain decoupling to transform the measured signal from the mechanical domain to the electrical domain to generate ECG measurement. Intuitively, it is reasonable that mechanical conduction and electrical conduction are highly correlated in describing cardiac activities because the electrical changes in cells trigger heart muscle contraction, whereas such a relationship is called excitation-contraction coupling in electrophysiology and is extremely hard to interpret or model by researchers without biological knowledge [21,33].

In the literature, the existing studies all leverage deep learning methods to extract latent information from enormous radar/ECG pairs and try to learn domain transformation relying on the extraordinary non-linear mapping ability of the deep

neural network [22, 29, 34–36]. Although these studies could successfully reconstruct the ECG signal from radar, there is no existing signal model with a compact form to describe the domain transformation for radar-based ECG reconstruction, and the well-trained deep learning model is not robust to abrupt noises such as RMB [22, 37], because these noises normally have orders of magnitude higher than cardiac-related vibrations, drowning out subtle features and ruining forward propagation of the deep neural network [38]. Therefore, the **second challenge** is to design the signal model that considers fine-grained cardiac features within a single cardiac cycle and design a robust single-cycle ECG generation module against abrupt noises.

### 1.3.3 The Third Challenge

After the modeling and recovery of single-cycle ECG pieces, a follow-up issue is to realize robust long-term ECG recovery. Although the model for the domain transformation between single-cycle radar/ECG pair has been proposed in [39], the long-term ECG recovery might be misaligned with ground truth due to inaccurate peak-to-peak interval (PPI) estimation, deteriorating the recovery quality even if the morphological features are well-recovered. Therefore, the **third challenge** is to model and generate the long-term ECG recovery from radar signal, and the recovery process should be robust against noises.

### 1.3.4 The Fourth Challenge

According to the literature, radar-based ECG recovery is only realized by deep-learning-based methods, because the domain transformation is extremely complex to be modeled mathematically while such transformation can be learned by deep learning model due to the great nonlinear mapping ability [22]. Similar to other research fields involved with deep learning, radar-based ECG recovery also asks for numerous radar signals to train the deep learning model with synchronous ECG ground truths [29, 40, 41]. According to previous research, the performance of the deep learning model degrades heavily after reducing 30% of the training data even after applying proper data augmentation techniques [42], causing difficulties for the

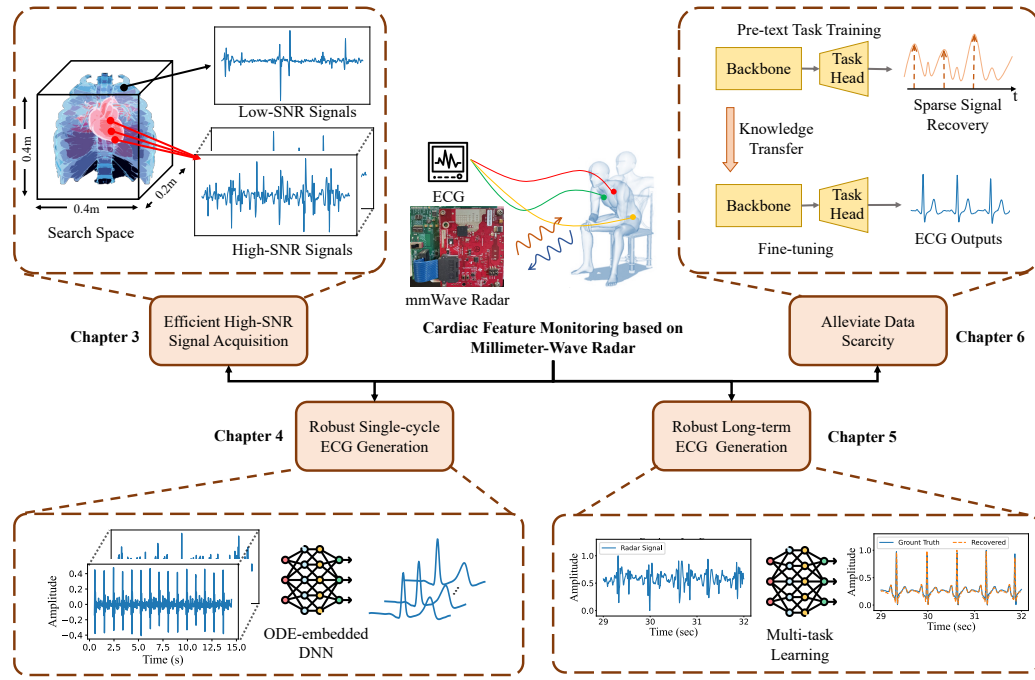


Figure 1.2: Overview of the thesis with unsolved challenges.

deployment in new scenarios due to the demand for hours of ECG collection [39]. However, the method for reducing dependence on data quantity is rarely investigated for radar-based ECG recovery, and all the deep-learning-based ECG recovery models are trained in a supervised manner with large dataset containing 3 – 32 hours of synchronous radar-ECG pairs [22, 29, 36]. In this case, the **fourth challenge** is to reduce the dependency on large-scale datasets and develop appropriate transfer learning or data augmentation methods to alleviate data scarcity, especially for the deployment in new scenarios with limited data.

## 1.4 Contributions and Thesis Outline

The proposed solutions for the aforementioned challenges are elaborated in Chapter 3, 4, 5 and 6 with a general outline shown in Figure 1.2, and the main contributions of this thesis can be concluded as:

- Chapter 3 proposes a cardio-focusing and -tracking (CFT) algorithm based on derivative-free optimization (DFO) to find the cardio-focused (CF) point by iteratively evaluating the potential points in a discontinuous objective space, with a universal signal template designed to adaptively assess the signal SNR as costs. The proposed CFT algorithm has been validated on sitting subjects in various scenarios and could provide radar measurements with better SNR compared with existing methods.
- Chapter 4 designs a signal model to describe the fine-grained cardiac feature sensed by radar, enabling further domain transformation between cardiac mechanical and electrical activities, instead of using purely data-driven approaches without any explanation as in the literature. Based on the proposed signal model, an ODE-embedded module called single-cycle ECG generator (SCEG) is designed to realize the domain transformation by parameterizing the radar signal into sparse representations and hence generate the morphological ECG features as references to resist noise.
- Chapter 5 investigates the noise robustness in radar-based ECG recovery against constant or abrupt noise by modeling the cardiac domain transformation as three tasks. An end-to-end multi-task learning (MTL) framework named radarODE-MTL is accordingly proposed to realize these tasks and leverage adjacent cardiac cycles to compensate for the distorted one. To assist the MTL model training, a novel optimization strategy called eccentric gradient alignment (EGA) is proposed for updating shared parameters in the MTL neural network, aiming to balance the intrinsic difficulty across tasks during network training and also prevent the negative transfer phenomenon.
- Chapter 6 tries to alleviate data scarcity in deep learning model training from two perspectives. Firstly, a transfer learning framework RFcardi is proposed following a self-supervised learning (SSL) paradigm to effectively learn the latent representations from radar signals by leveraging an appropriate pre-text task. Secondly, a data augmentation method called Horcrux is proposed to expanding

the diversity of the limited training dataset without distorting the intrinsic time consistency hidden in the radar inputs.

In addition, Chapter 2 provides the necessary background for radar-based vital sign monitoring, and Chapter 7 concludes the entire thesis with several promising research directions for future investigation.

# **Chapter 2**

## **Background and Literature Review**

In this chapter, the necessary background for radar theory and radar-based vital sign monitoring is first provided for a better understanding of the proposed methods in the later chapters. In addition, the representative signal processing methods for cardiac feature extraction are also introduced to provide a comprehensive review of the development over the last decade.

### **2.1 Background for Radar-based Cardiac Monitoring**

### **2.2 Literature Review**

# Chapter 3

## High-SNR Radar Signal

### 3.1 Introduction

Radio detection and ranging (radar) system is originally designed for military detection of large aircraft by emitting electromagnetic waves and evaluating the reflections. The follow-up research has investigated the civilian use of radar systems for contactless sensing in various scenarios, such as autonomous driving [43] and human monitoring [2]. Over the past decade, radar-based sensing has been empowered by deep neural networks to process non-stationary reflected signals or high-dimensional data, enabling versatile applications to replace contact- or visual-based measurement for convenience or privacy concerns (e.g., vital sign monitoring [23], gesture recognition [44], fault diagnosis [45]).

Radar-based vital sign monitoring, as a popular branch of radar-based sensing, has been explored for decades to measure heart rate or respiration rate in a contactless manner [2], and some further studies leverage the deep neural network to realize domain transformation from cardiac mechanical activities (i.e., heartbeat) to electrical activities (i.e., electrocardiogram (ECG)), providing a fine-grained cardiac measurement for wellness monitoring or clinical diagnosis [22, 29, 34, 39, 40, 42, 46]. In the literature, radar-based ECG recovery is only realized by deep-learning-based methods, because the domain transformation is extremely complex to be modeled

mathematically while such transformation can be learning by deep learning model due to the great nonlinear mapping ability [22].

Similar to other research fields involved with deep learning, radar-based ECG recovery also asks for numerous radar signals to train the deep learning model with synchronous ECG ground truths [29, 40, 41]. According to previous research, the performance of the deep learning model degrades heavily after reducing 30% of the training data even after applying proper data augmentation techniques [42], causing difficulties for the deployment in new scenarios due to the demand for hours of ECG collection [39]. However, the method for reducing dependence on data quantity is rarely investigated for radar-based ECG recovery, and all the deep-learning-based ECG recovery models are trained in a supervised manner with large dataset containing 3 – 32 hours of synchronous radar-ECG pairs [22, 29, 36].

In contrast, most studies are dedicated to inventing advanced signal processing algorithms to enhance the signal quality, because the deep learning model for ECG recovery is vulnerable to the inputs contaminated by noises and requires high signal-to-noise ratio (SNR) radar signals as inputs [22, 23]. The methods for capturing high-SNR radar signals can be categorized into two groups:

- The first type of method focuses on designing advanced radar front-end with multiple transmitters (Tx) and receivers (Rx) [24, 25] or calibrating baseband radar signals from in-phase and quadrature (IQ) channels to a circular shape [26–28].
- The second type of method assumes that the rough localization of human body provides accurate chest region with the majority of range bins containing useful cardiac features, and high-SNR signal can be obtained by selecting useful bins/channels/antennas [29, 30], applying clustering algorithms [22] or accumulating the signals from various dimensions (e.g., chirps, frames, antennas) [23].

The first type of method is not suitable for some commonly used frequency-modulated continuous-wave (FMCW) radar platforms (e.g., TI AWR-x radar) due to the on-board digital front-end module filtering the frequency-modulated feature of baseband signal (i.e., circular IQ plot) [31], preventing the broad applications of

this approach in commercial radar. The second type of method relies on accurate localization of the chest region, while the existing methods only provide a rough location of the human body, causing a deviation of several decimeters due to different postures of the subject [32]. Therefore, the methods based on signal accumulation may fail because only a minority of range bins contain cardiac features, hence not subjecting to the law of large numbers [23]. Although some aforementioned studies have proposed methods for selecting or clustering the useful range bins with cardiac features [22, 29], the computational cost for traversing a large objective space can be huge without an accurate cardiac location.

Based on the above discussion, it is still a challenge to: (a) precisely locate and track the cardiac location during data collection to efficiently extract high-SNR radar signal; (b) develop a deep learning framework for radar-based ECG recovery, with less demand for ECG collection and realizing an efficient model training especially for new scenarios with limited data. To overcome these two challenges, the contributions of this study can be listed as:

- A cardio-focusing and -tracking (CFT) algorithm is proposed based on derivative-free optimization (DFO) to find the cardio-focused (CF) point by iteratively evaluating the potential points in a discontinuous objective space, with a universal signal template designed to adaptively assess the signal SNR as costs.
- A transfer learning framework RFcardi is proposed following a self-supervised learning (SSL) paradigm to effectively learn the latent representations from radar signals by leveraging an appropriate pre-text task. Accordingly, this work further designates the sparse signal recovery (SSR) as the pre-text task, assisting the RFcardi to learn essential representations for the later ECG recovery.
- The proposed CFT algorithm has been validated on sitting subjects in various scenarios and could provide radar measurements with better SNR compared with existing methods. In addition, the pre-trained RFcardi framework can be easily adapted to realize radar-based ECG recovery with a small amount of synchronous radar-ECG measurements for fine-tuning.

The rest of the paper is organized as follows. Section 3.2 provides the background information for radar-based ECG recovery and SSL. Section 3.3 elaborates the proposed CFT algorithm and RFcardi framework, with the experimental settings and results shown in Section 3.4 and 3.5. The final conclusion is shown in Section 3.6.

## 3.2 Theoretical Background and Challenges

### 3.2.1 FMCW Radar Foundations

FMCW radar has been widely used in nowadays millimeter-wave (mmWave) sensing to measure the range, velocity and angle of arrival (AoA) of the objects appearing in the field of view [47], with three critical concepts that configure the transmitted waveform:

- **Chirp** is the minimum component in the FMCW signal with microsecond-level duration and is often called fast time. The waveform of a single chirp is a sinusoidal signal with frequency that changes linearly over time, with the key characteristics designated by start frequency, bandwidth and chirp duration to get range information of the object.
- **Frame** is a collection of multiple chirps that forms a complete observation window to get the velocity information based on the range bins extracted from chirps and is often referred to as slow time.
- **Virtual antenna array (channel)** is a commonly used concept in multiple-input and multiple-out (MIMO) radar systems and is able to realize complex modulations or beamforming [25]. However, this study mainly leverages the phase difference across antenna channels to estimate the AoA of the objects.

The popular commercial radar platforms have provided a convenient interface for radar configuration, signal modulation and demodulation [48]. Therefore, detailed equations of FMCW radar signal processing might be redundant in this paper, while the theoretical explanation can be found in previous papers [47, 49].

### 3.2.2 Cardiac Signal Extraction from FMCW Radar

ECG recovery relies on the high-SNR radar inputs that describe the mechanical cardiac activities, and the reflected signal from a given point  $E = (x, y, z)$  in 3D space can be expressed as:

$$R(E, t) = \sum_{v=1}^V \sum_{c=1}^C \sum_{n=1}^N s_{v,c,n}(t) \cdot e^{j2\pi \frac{2k \cdot d(E, v)}{\text{light speed}} n} \underbrace{e^{j2\pi \frac{2 \cdot d(E, v)}{\lambda}}}_{\text{phase term } \phi} \quad (3.1)$$

where  $(x, y, z)$  represents the (horizontal, radial, vertical) axis,  $V$  is the number of virtual antenna channels,  $C$  means the number of chirps within one frame,  $N$  is the total sample points within one chirp,  $s_{v,c,n}(t)$  denotes the original received signal,  $k$  is the slope of frequency raising,  $\lambda$  means wavelength and  $d(E, v)$  represents the distance between point  $E$  and virtual antenna  $v$  [22]. In FMCW processing for vital sign monitoring, the time sample  $t$  corresponds to one frame instead of the sample point  $n$ , and the signal from different chirps  $c$  and antenna channels  $v$  will be accumulated to improve SNR [23].

The interested term in (3.1) is the variation of distance  $d(E, v)$ , because it represents the displacements caused by respiration and heartbeat (without considering any other noise). Therefore, the chest region displacement  $h(E, t)$  can be unwrapped from phase variation  $\Delta\phi$  as

$$h(E, t) = \frac{\lambda\Delta\phi}{4\pi} \quad (3.2)$$

At last, some common noises, such as respiration and thermal noise, can be easily removed using a band-pass filter and differentiator to make sure that the final  $h(E, t)$  mostly contains cardiac-related features from point  $E$  as shown in Figure 3.1(a).

**Challenge:** It is natural to think the high-SNR radar signal can be searched in a constrained space by optimization, while there is no appropriate method to assess the signal SNR in terms of cardiac features contained, and the objective space is actually highly discontinuous with adjacent points may revealing totally different SNR as shown in Figure 3.1(a) and 3.1(b), restricting the application of common gradient-based optimization algorithms.

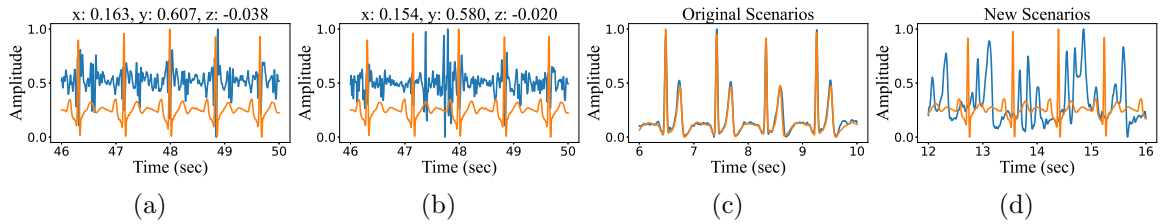


Figure 3.1: Challenges for radar-based ECG recovery: (a) and (b) Radar signals with high and low SNR for adjacent points with a distance of 0.03m; (c) and (d) Inference results of a well-trained deep learning model in original and new scenarios.

### 3.2.3 Transfer Learning

In addition to high-SNR radar inputs, accurate ECG recovery also relies on the scale of datasets to train the deep learning model, with the previous research normally adopting the dataset with the length of 3 – 32 hours [22, 29, 36]. Unfortunately, the initial experimental results show that the well-trained deep learning model cannot be directly used for the signal collected from new scenarios even using a similar radar configuration as shown in Figure 3.1(c) and 3.1(d), because different in-door scenarios and radar configurations may have unknown interference on radar signals [2].

Inspired by other signal-based research [30, 50], transfer learning is a promising paradigm to learn the latent representation from unlabeled radar signal to capture basic cardiac features in an SSL manner, reducing the requirement of cumbersome ECG collection. Then, only a small amount of synchronous radar-ECG pairs is required to fine-tune the pre-trained model to realize the ECG recovery for new scenarios.

**Challenge:** The efficient SSL requires an appropriate design of the pre-text task to help the deep learning model capture essential features that assist ECG recovery, while no existing work has investigated only learning from radar signals without the aid of ECG ground truth.

## 3.3 Methodology

### 3.3.1 Overview of CFT-RFcardi Framework

The pipeline of the proposed CFT-RFcardi framework is shown in Figure 3.2 with three steps:

- The received radar signal will be converted into a standard format in terms of chirp, frame and virtual antenna channel to obtain the general location of the subject, as shown in Figure 3.2(a).
- The rough location acts as the initial state for the CFT algorithm, and the points within a constrained space will be evaluated to find the red CF point with best SNR as shown in Figure 3.2(b).
- Signals extracted from the ten best points will be converted into spectrograms to pre-train the backbone with SSR as the pre-text task. Then, the same backbone will be used for the fine-tuning stage so that the latent representations learned in the pre-trained model can be seemly transferred for the ECG recovery task, as shown in Figure 3.2(c).

In addition, TI-AWR 1843 radar operated at 77 Ghz with 2 Tx and 4 Rx will be used for data collection, enabling 8 virtual antenna channels for high-quality signal extraction. The detailed scenario descriptions and radar configurations will be provided in Section 3.4.1.

### 3.3.2 Rough Localization

The received radar signal is first formatted as a standard data matrix in terms of different chirps, frames and virtual channels to provide measurement of range, velocity and AoA, respectively. For the current research level of radar-based vital sign monitoring, the subjects are all quasi-static without velocity, and only the range-angle (RA) map will be calculated using fast Fourier transform (FFT) as shown in Figure 3.2(a), with a detailed illustration of signal waveform and processing shown in Figure 3.3.

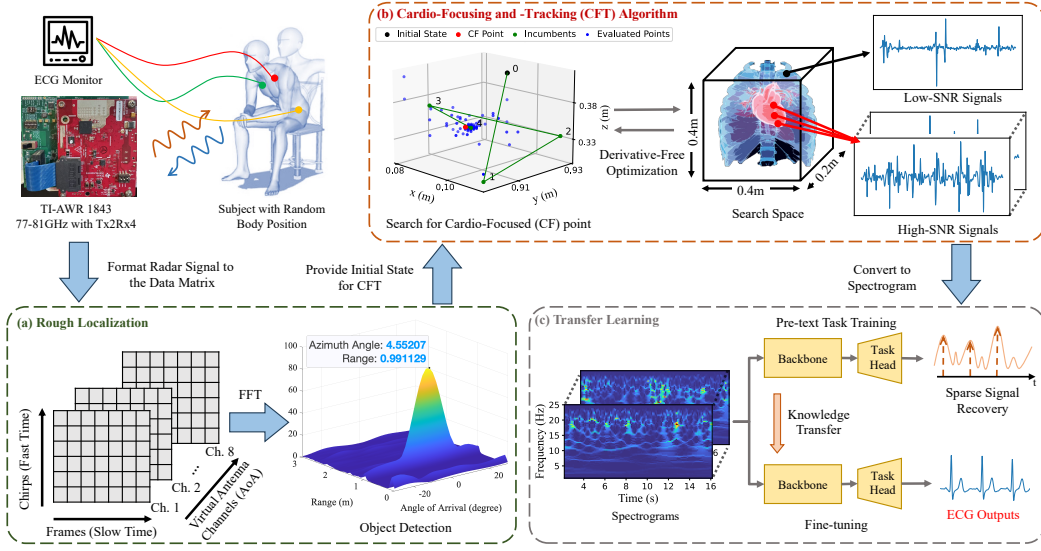


Figure 3.2: Overview of the CFT-RFcardi framework: (a) Rough localization of human body; (b) Use CFT to find CF point and extract high-SNR radar signals; (c) Transfer learning with pre-text task training and fine-tuning stages.

### Range FFT

According to (3.1), the signal propagation after transmitting introduces a constant phase shift  $\phi_s$  in the received signal and is expressed as

$$\phi_s = \frac{4\pi d_0}{\lambda} \quad (3.3)$$

with  $d_0$  representing the distance between radar and human body. Therefore, the distance  $d_0$  can be extracted from each received signal along fast time using FFT as shown in Figure 3.3(a), and the updated data matrix now reveals the range information, i.e., a static object denoted as blue along slow time axis.

### Angle FFT

The ability of AoA detection relies on the MIMO system using time division multiplexing (TDM-MIMO), with multiple Tx alternately transmitting chirp signals and the corresponding reflections can be distinguished during receiving as shown in Fig-

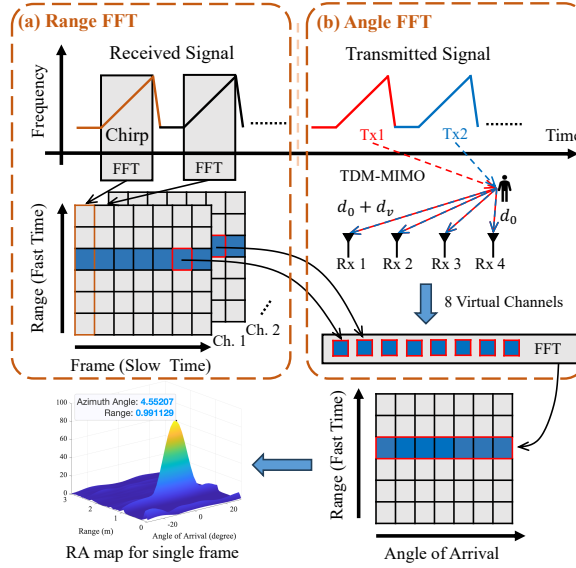


Figure 3.3: Procedures for obtaining RA map: (a) Range FFT for chirps along fast time; (b) Angle FFT along virtual channels.

ure 3.3(b). Due to the physical distance varies for different Tx/Rx combinations (i.e., Tx2Rx4 creates 8 virtual channels), an extra propagation  $\Delta\phi_v$  delay will be introduced as:

$$\Delta\phi_v = \frac{4\pi d_v}{\lambda} \quad (3.4)$$

$$d_v = l \sin(\theta)$$

where  $d_v$  represents the extra propagation distance,  $l$  means the distance between adjacent antenna channels and  $\theta$  is the incident angle. Similar to range FFT, the phase differences across different channels can be used to extract AoA information for each range bin by performing FFT along the channel axis, as shown in red squares in Figure 3.3(b).

After combining the FFT results for all chirps and channels, the final RA map for the current time sample (frame) can be obtained as shown in Figure 3.3. The same procedure can be repeated along the slow time axis to get the rough human body location for all the time samples, but this study only requires the location obtained from the very first frame as the initial point  $E_0$  for CFT algorithm.

### 3.3.3 Cardio-focusing and -tracking (CFT) Algorithm

The radar signal for any point can be extracted following (3.1) and (3.2), and the search progress from  $E_0$  to the best point  $E_b$  (i.e., CF point with high SNR) requires: (a) an appropriate metric to assess whether the radar signal contains wanted cardiac features; (b) an optimization method that is applicable to the discontinuous objective space based on the assessed SNR values as costs.

#### Template Design for Assessing SNR

An explicit SNR can be calculated with the known “clean” signal, while the “clean” signal for vital signs normally reveals two prominent vibrations corresponding to the ventricular contraction and relaxation [39], as shown in Figure 3.4(a). However, considering the vibrations may have subtle differences due to different scenarios or radar configurations (e.g., noise figure and sampling frequency), a universal template  $h_m$  is designed in this study to fit the envelope of the radar signal as:

$$h_m(t) = a_1 \exp\left(-\frac{(t - b_1)^2}{2c_1^2}\right) + a_2 \exp\left(-\frac{(t - b_2)^2}{2c_2^2}\right) \quad (3.5)$$

with  $a_1, a_2$  controlling the amplitudes of the peaks,  $b_1, b_2$  determining the centers of the peaks and  $c_1, c_2$  adjusting the width of the peaks. In practice,  $a_1$  and  $b_1$  will be fixed based on the dominant peaks detected as the red points in Figure 3.4(b), and other parameters are left to be determined as a simple curve fitting problem. Finally, the mean square error (MSE) between the radar signal envelope and the synthetic template is reckoned to be an assessment of signal SNR as shown in Figure 3.4(b), because fewer components could fit the designed template for low-SNR radar signal without obvious cardiac features, as shown in Figure 3.4(c) and 3.4(d).

#### Derivative-free Optimization (DFO)

The MSE values obtained from template matching for the radar pieces extracted from point  $E$  will be used as costs  $\mathcal{F}(E)$  in searching CF point, but the traditional gradient-based optimization method is not applicable because there is no explicit cost

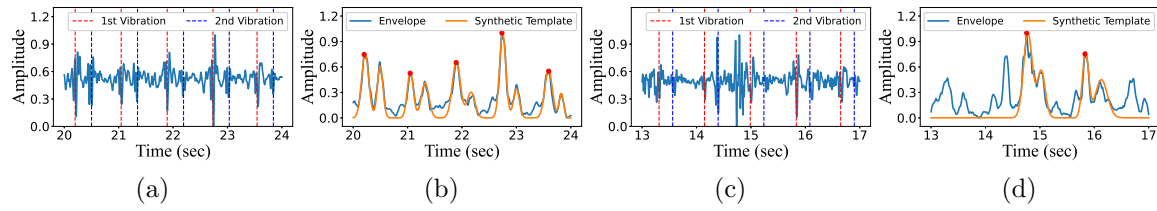


Figure 3.4: Template for assessing SNR: (a) High-SNR radar signal; (b) Extracted signal envelope with the synthetic template; (c) (a) Low-SNR radar signal, (d) Extracted signal envelope with the synthetic template.

function. Therefore, the CFT algorithm is developed in a derivative-free manner based on coordinate search (CS) algorithm [51], to asymptotically approach the CF point.

The definition of the DFO problem is formulated as:

$$E_b = \arg \min_{E \in \mathbb{R}^n} \{\mathcal{F}(E) : E \in \Omega\} \quad (3.6)$$

with  $\Omega$  representing a user-defined constrained  $n$ -dimensional search space near initial point  $E_0$  as shown in Figure 3.2(b), and the cost of points out of the constraint will be set as  $\mathcal{F}(E \notin \Omega) = \infty$ . During each iteration  $k$ , many trial points  $E_k$  within the constraint will be evaluated to find the incumbent points  $E_i$  as the temporary best point for the next iteration.

To perform a derivative-free search, the traditional CS algorithm starts from the initialization of grids  $G_k$ :

$$G_k := \{E_k + \gamma_k D\} \subset \mathbb{R}^n \quad (3.7)$$

where  $\gamma_k > 0$  is the grid size parameter and  $D$  contains several vectors  $p$  for possible searching directions, as shown in Figure 3.5(a). The local convergence of CS is ensured by dense search directions  $D$  and a refined grid size  $\gamma_k$  to find better  $E_i$  compared with current  $E_k$  [51]. However, the highly discontinuous objective space for radar-monitored vital signs may have numerous local minima that distract the optimization algorithm, i.e., the signal SNR of the adjacent points might be very different, as shown in Figure 3.1(a) and 3.1(b).

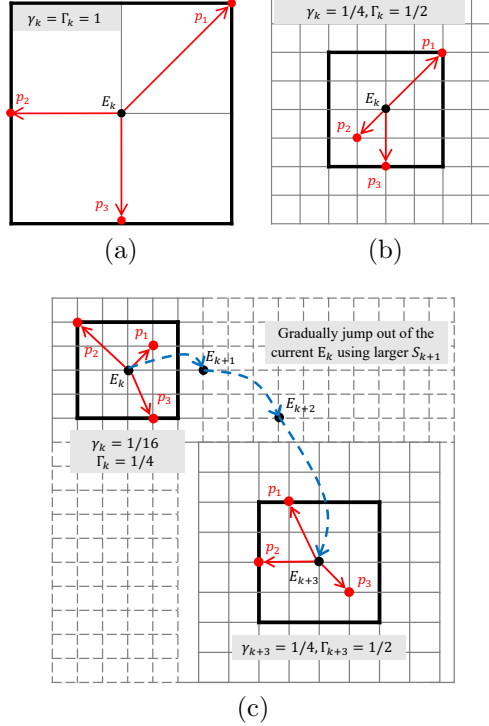


Figure 3.5: Illustration of the CFT algorithm with bold line wrapping the search region  $S_k$ : (a) Equality between  $\gamma$  and  $\Gamma$  (same as in CS algorithm); (b) Large  $\Gamma_k$  with refined  $\gamma_k$ , providing more potential points to be evaluated; (c) Jump out of the local minimum by adjusting  $\Gamma_k$  and  $\gamma_k$ .

To jump out of the potential local minimum, CFT algorithm is proposed by introducing search region  $S_k$  to restrict the possible search directions  $p$ , alleviating the difficulty of searching in numerous dense grid points and allowing the adjustment of search region and grid size iteratively to break the local minimum. The detailed procedures of CFT are shown in Algorithm 1, with an illustration of  $\mathbb{R}^2$  space shown in Figure 3.5.

In CFT, the grids  $G_k$  is still expressed as in (3.7) and the newly introduced search region  $S_k$  is expressed as:

$$S_k := \{E \in G_k : \|E - E_k\|_\infty \leq \Gamma_k a\} \quad (3.8)$$

with  $a = \max \{\|a'\|_\infty : a' \in D\}$  and  $\Gamma_k$  as the size parameter for the search region. An intuitive interpretation of  $S_k$  is the point set that contains grid points inside and on the boundary of the bold line controlled by  $\Gamma_k$ , as shown in Figure 3.5(b).

Based on the well-constructed grids  $G_k$  and search region  $S_k$ , the remaining CFT algorithm is performed with searching and resizing stages:

**Searching:** The searching stage simply asks for the evaluation of  $\mathcal{F}(E)$  on a subset of grids  $G_k$  based on any sampling algorithm (e.g., Latin hypercube sampling [51]), as indicated in line 6 in Algorithm 1.

**Resizing:** The resizing stage depends on the result of searching stage:

- If a new incumbent point  $E_i$  is found with better SNR, the search region will be doubled as  $\Gamma_{k+1} = 2\Gamma_k$  (line 8), and the grid size will be empirically set as  $\gamma_{k+1} = \min(\Gamma_k, \Gamma_k^2)$  (line 16), enabling to search in broader space in the next iteration.
- If there is no better point than the current  $E_k$  on the current grids  $G_k$ , another searching stage will be performed only within the search region  $S_k$  (line 9). Then, If a better point  $E_i$  is found,  $\Gamma_{k+1}$  and  $\gamma_{k+1}$  is obtained as above (line 11), otherwise, the search region will be halved as  $\Gamma_{k+1} = \Gamma_k/2$  (line 14) for a finer search with  $\gamma_{k+1} = \min(\Gamma_k, \Gamma_k^2)$  (line 16).

The searching step enables the finding of better points  $E_i$  in a broad space, and the resizing step either refines the grid if the current  $\gamma_k$  is not enough or enlarges the search space when stalling at the local minimum, as shown in Figure 3.5(c). Finally, the CFT algorithm will be terminated after achieving a desired  $\text{SNR}_d$  or iteration limit  $k_{max}$ .

The visualization of the CFT algorithm in Figure 3.2(b) shows that initial iterations search in a large space, and the algorithm could jump out of the green local minima to find the red CF point within the fine blue grid points. In addition, the tracking of the CF points along time can be naturally realized by repeating Algorithm 1 with previous  $E_b$  as the new  $E_0$ , and the SNR evaluated on the previous point might have already achieved  $\text{SNR}_d$  due to the quasi-static human body, sav-

**Algorithm 1** CFT Algorithm

---

```

1: Input:  $E_0$ ,  $\text{SNR}_d$ ,  $k_{max}$ 
2: Output:  $E_b$ ,  $\text{SNR}_b$ 
   OBJECTIVE:
3:  $E_b = \arg \min_{E \in \mathbb{R}^n} \{\mathcal{F}(E) : E \in \Omega\}$ 
4: Initialize  $k = 0$ ,  $\Gamma_k = \gamma_k = 1$ ,  $\text{SNR}_b = \mathcal{F}(E_k)$ 
5: while  $\text{SNR}_b > \text{SNR}_d$  and  $k < k_{max}$  do
6:   if  $\mathcal{F}(E) < \text{SNR}_b$  for some  $E \in G_k$  then
7:      $E_{k+1} \leftarrow E$ ,  $\text{SNR}_b \leftarrow \mathcal{F}(E)$ 
8:      $\Gamma_{k+1} \leftarrow 2\Gamma_k$ 
9:   else if  $\mathcal{F}(E) < \text{SNR}_b$  for some  $E \in S_k$  then
10:     $E_{k+1} \leftarrow E$ ,  $\text{SNR}_b \leftarrow \mathcal{F}(E)$ 
11:     $\Gamma_{k+1} \leftarrow 2\Gamma_k$ 
12:   else
13:      $E_{k+1} \leftarrow E_k$ 
14:      $\Gamma_{k+1} \leftarrow \Gamma_k/2$ 
15:   end if
16:    $\gamma_{k+1} \leftarrow \min(\Gamma_k, \Gamma_k^2)$ 
17:    $k \leftarrow k + 1$ ,  $E_b \leftarrow E_{k+1}$ 
18: end while

```

---

ing a huge amount of time for calculating useless channel information for filtering or clustering [22, 23, 29].

### 3.3.4 Transfer Learning for ECG Recovery

#### Deep Learning Model Design

The radar signal extracted from the 10 best points from CFT algorithm will be converted to spectrograms as the input for deep learning model according to our previous work [40], providing extra frequency-domain information to assist model training. The deep learning model adopts the popular backbone-decoder structure as designed in [40]:

- The backbone leverages ResNet [52] framework with deformable 2D convolution layer [53] to efficiently extract cardiac features from image-like spectrogram

inputs.

- The decoder is based on 1D convolutional neural network (CNN) to generate corresponding signals either for the pre-text task or ECG signal recovery.

### Pre-text Task Training and Fine-tuning

The pre-text task used for SSL should reveal certain inherent features in the radar-monitored vital sign, and two major features used for traditional heart rate estimation are periodicity and sparsity [2]. In this work, the duration of each segment is 4 sec and may not reveal strong periodicity. Therefore, SSR will be used as the pre-text task in RFcardi and is defined as:

$$h = \Phi x + n \quad (3.9)$$

where  $h$  is the high-SNR radar signal,  $\Phi$  means the observation matrix,  $x$  is the sparse representation for heartbeats and  $n$  represents the residual noise. The traditional SSR task can be seemly converted to a system identification problem by viewing  $\Phi$  as a multi-channel adaptive filter, and the estimation of the filter coefficient is the same as training a CNN-based neural network (i.e., training CNN kernels) [15].

In this case, the SSR task is realized by using the aforementioned CNN-based backbone-decoder structure with the loss function:

$$\mathcal{L} = \|x - x'\|_2 + \lambda_s \underbrace{\frac{\|x\|_1/\|x\|_2 - 1}{\sqrt{m} - 1}}_{\text{sparse penalty}} \quad (3.10)$$

where  $m$  is the length of the signal,  $x$  is the output the from deep learning model,  $x'$  is the sparse ground truth with values for the radar peaks maintained (1st vibration in Figure 3.4(a)) while other values are set to 0. The sparse penalty has a range of  $[0, \lambda_s]$  with a smaller value indicating better sparsity [54].

After pre-training based on SSR, the parameters of backbone will be retained with a new decoder connected (same structure as for pre-text task training), and a



Figure 3.6: Indoor scenarios for data collection.

few radar-ECG pairs are used for fine-tuning the pre-trained RFcardi model using MSE as the loss function.

## 3.4 Details of Experiment and Dataset

### 3.4.1 Experimental Details

#### Dataset Collection and Preparation

The dataset contains a total of 80-minute synchronous radar-ECG pairs collected for 5 healthy subjects (3 men, 2 women) in 2 indoor scenarios as shown in Figure 3.6. The subjects are asked to sit causally and are allowed to change postures during data collection, and each data trial lasts for 1 minute. The distance between radar and human body varies from 0.5–1.2m, and a longer distance causes the decrease of signal SNR with a smaller portion of the space points containing useful cardiac features.

TI-AWR 1843 radar with 2 Tx and 4 Rx is used for data collection with 8 virtual antenna channels created [48], and the radar configurations are listed in Table 3.1 with the name provided in TI mmWave-Studio interface. The signal will be sampled as 200Hz, and only a band-pass filter from 0.5 to 50Hz and a differentiator are used for removing respiration noise because the radar signal extracted from CF points already has high SNR. Lastly, the ECG ground truth is collected using TI ADS1292, and the related ECG processing (e.g., smoothing and peak finding) is realized by NeuroKit2 python package [55].

Table 3.1: Parameters for data collection interface

Parameter	Value	Parameter	Value
Start Frequency	77GHz	Frequency Slope	65MHz/ $\mu$ s
Idle Time	10 $\mu$ s	Tx Start Time	1 $\mu$ s
ADC Start Time	6 $\mu$ s	ADC Samples	256
Sample Rate	5000kbps	Ramp End Time	60 $\mu$ s
Start/End Chirp Tx	0/2	No. of Chirp Loops	2
No. of Frames	12000	Frame Periodicity	5ms

### 3.4.2 Implementation Details

#### Parameters for CFT Algorithm

The constraint  $\Omega$  for the CF point search is centered at the initial state  $E_0$  with a range of  $0.4 \times 0.2 \times 0.4$ m as illustrated in Figure 3.2(b). In addition, the initial grid and search region size should be adjusted to fit the real-life physical unit as  $\Gamma_k = \gamma_k = 0.1$ m, and the size will be limited as  $\Gamma_k \geq \gamma_k \geq 0.001$ m to prevent an exhaustive search within a meaningless small space. At last,  $\text{SNR}_d$  is set to 0.01 for the desired MSE between normalized synthetic template and signal envelope, and  $k_{max}$  is set to 100.

#### Deep Learning Model Training

The deep learning model adopts the same backbone, ECG decoder and hyperparameters as in our previous open-sourced work [40] coded in PyTorch and trained on NVIDIA RTX 4090 (24GB). The total training epoch is set to 100 with batch size 8, and a 5-fold cross-validation training strategy is adopted to split the dataset to make the most of the limited dataset while excluding the testing data from the training phase. The parameter for balancing the weight of sparse penalty is set as  $\lambda_s = 0.1$ .

### 3.4.3 Methods for Comparison

The comparison is performed with the representative methods based on accumulation and clustering to extract high-SNR radar signal:

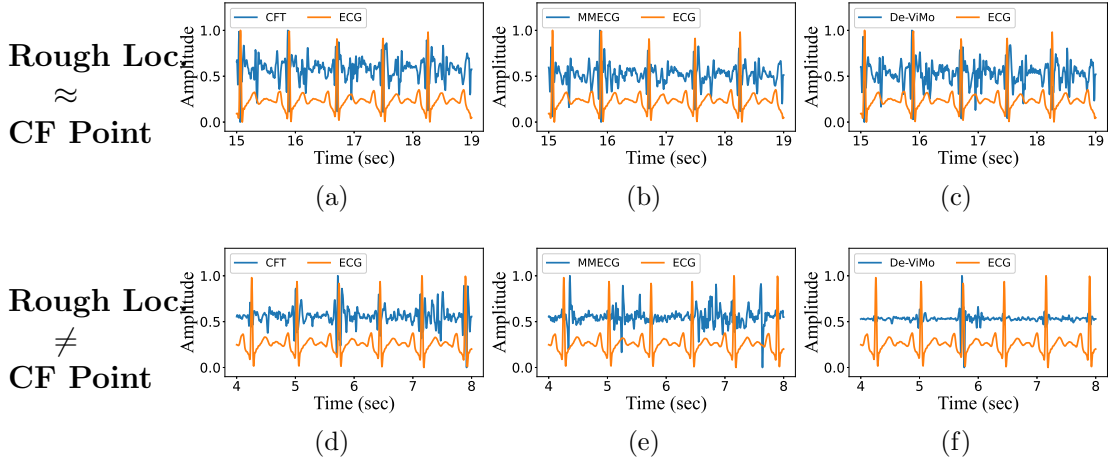


Figure 3.7: Visualization of the extracted radar signal for all methods: (a) - (c) If CF point is around rough body location; (d) - (f) If CF point is far from rough body location.

- De-ViMo [23] is proposed for heart rate monitoring and is based on the accumulation of signals from various dimensions (e.g., chirps, antennas, spatial points) to enhance cardiac features while mitigating noise. In addition, De-ViMo also improves the rough localization by identifying the peaks in micro-motion frequency bands instead of the entire FMCW bands.
- MMECG [22] requires the calculation of numerous points in 3D space and applies clustering algorithm to improve SNR. Then, a pattern-matching process is performed to learn the common pattern from the clustered result and select the best radar signal(s).

In addition, to the best of our knowledge, this is the first paper that leverages SSL with an appropriate pre-text task for pre-training of radar-based ECG recovery, and only the performance analysis will be provided without comparison with other methods.

## 3.5 Experimental Results and Evaluations

### 3.5.1 Performance of CFT Algorithm

#### Effectiveness of CFT Algorithm

The examples of the extracted radar signal for different methods are shown in Figure 3.7, illustrating that precise cardiac localization has a huge effect on the signal quality. For example, if the rough body location is around CF point, all three methods can obtain high-SNR signals with clear first and second vibrations using either space search (CFT, Figure 3.7(a)), clustering (MMECG, Figure 3.7(b)) or accumulation (De-ViMo, Figure 3.7(c)).

In contrast, only a few range bins will contain useful cardiac features if the rough body location is far from CF points, especially when increasing the monitoring range. Therefore, the signal accumulation may enhance the noises as shown in Figure 3.7(f) while the signal clustering may also encounter a failure due to the lack of homogeneous cardiac signals as shown in Figure 3.7(e). However, The proposed CFT could precisely locate the CF point with good SNR subject to the designed signal template and DFO searching strategy, and the extracted radar signal still shows clear peaks as shown in Figure 3.7(d).

During the data collection of this study, the subjects are allowed to change postures to alleviate discomfort, with a resultant CF point deviation of several decimeters, while the rough location provided by FMCW signal processing is still unchanged. Therefore, the proposed CFT algorithm is essential because the posture change is inevitable, and a thorough evaluation in terms of different monitoring ranges will be performed in the next part.

#### Impact of Monitoring Range

To evaluate the performance of different methods when increasing the monitoring range, the quality of extracted radar signals for all trials is evaluated in terms of:

- Absolute Peak error between ECG R peaks and the dominant peaks for the first

vibrations in radar signal.

- Missed detection rate (MDR) to count the cardiac cycles with no peak detected or with the absolute peak error larger than 150ms [22].

Figure 3.8(a) and 3.8(b) illustrate the peak error and MDR for all 80 trials with corresponding fitting curves indicating the mean peak error or MDR. All the methods show similar performance in the short range and experience certain degradation with respect to the increasing range. In particular, MMECG shows larger degradation and variance for longer-range cases because the rough localization based on FMCW signal processing cannot provide accurate cardiac location, and the resultant evaluated points may not capture useful information for clustering. In contrast, De-ViMo could provide a better cardiac location, and the accumulated results show better accuracy than MMECG, while the long-range monitoring still affects the quality because the accumulation is not robust to non-gaussian noise. At last, the proposed CFT could precisely focus on the CF point and keep tracking the high-SNR points during data collection, providing the best results with small variance for both peak error and MDR.

In addition, the cumulative distribution function (CDF) plots for all trials are shown in Figure 3.8(c) and 3.8(d). The proposed CFT algorithm achieves the best peak error with a median value of 0.022 sec, while DE-ViMo and MMECG have worse performances with larger median values of 0.028 sec and 0.033 sec, respectively. Similarly, the precise localization and tracking of CF point also reduces the MDR for CFT results with a median value of 14%, while DE-ViMo and MMECG may affected by the accumulated noise or inaccurate cardiac localization with the median MDR of 17% and 23%, respectively.

### Impact of Signal Quality on ECG Recovery

The signals extracted using different methods are used for supervised training to verify the impact of different input qualities on the ECG recovery task. The quality of the recovered ECG signal is assessed in terms of:

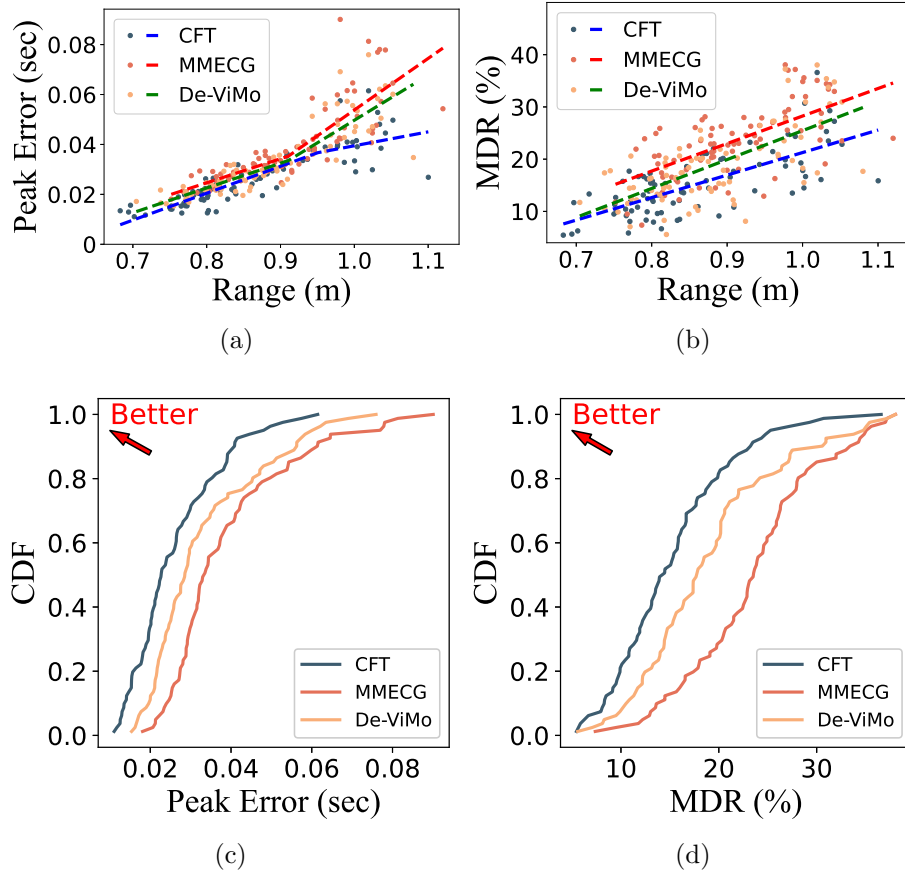


Figure 3.8: Illustration of performance in terms of peak error and MDR: (a) - (b) Scattered points with fitting curves along range axis; (c) - (d) CDF plots for all trails.

- The morphological accuracy is measured using MSE and Pearson-correlation coefficient (PCC), with MSE sensitive to the peak deviation and PCC focusing on the similarity between the ECG patterns.
- The accurate recovery of ECG R peaks is crucial to coarse cardiac features calculation (e.g., heart rate variability) and is measured by absolute R peak error and MDR.

Table 3.2 shows the performance of the deep learning model trained with datasets yielded by different methods. The training based on CFT dataset achieves the best

Table 3.2: Performance of supervised ECG recovery

Methods	MSE ( $\times 10^{-2}$ ) ↓	PCC ↑	Peak Error (ms) ↓	MDR ↓
MMECG [22]	0.93	80.36%	9.74	7.96%
De-ViMo [23]	0.88	83.83%	8.93	7.32%
CFT	<b>0.82</b>	<b>85.47%</b>	<b>7.61</b>	<b>6.85%</b>

Table 3.3: Performance of SSL with ablation study

Methods	MSE ( $\times 10^2$ ) ↓	Sparsity ↓	MSE ( $\times 10^2$ ) ↓	Sparsity ↓
	<b>100% Dataset</b>			
SSL w/o sp*	0.91	0.36	0.96	0.41
SSL with sp	0.82	0.20		
	<b>60% Dataset</b>		<b>40% Dataset</b>	
	SSL w/o sp	1.43	0.44	Failed
SSL with sp	0.92	0.26	0.98	0.31

\*sp for sparse penalty

results on both morphological accuracy (MSE= 0.0082 and PCC= 85.47%) and R peak recovery (Peak Error= 7.61ms and MDR= 6.85%), because the high-SNR inputs provide accurate peak locations with minor noise that affects the ECG pattern generation, as shown in Figure 3.9(a) and 3.9(b).

In contrast, MMECG and De-ViMo cannot preserve the signal quality especially for long-distance cases, and the noisy inputs will prevent the deep learning mode from identifying the accurate position of ECG pieces, causing large peak error and MDR, as shown in Figure 3.9(c) and 3.9(d). It is worth noticing that poor signal SNR causes more degradation in peak error than morphological accuracy, because the ECG patterns share a similar shape and can be learned from other cardiac cycles, while the peak recovery (detection) fully relies on the current radar input and can be ruined by noises.

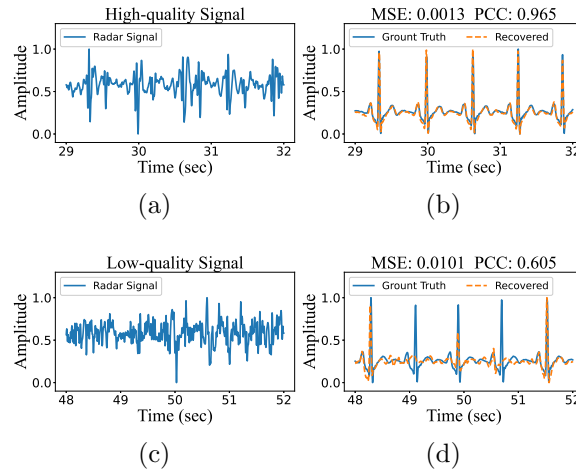


Figure 3.9: Impact of radar input quality on the final ECG recovery: (a) - (b) High-quality radar input and ECG recovery; (c) - (d) Low-quality radar input and ECG recovery.

### 3.5.2 Performance of ECG Recovery using Transfer Learning

#### Evaluations and Ablation Studies of SSL

The SSR task is crucial in the proposed transfer learning framework to provide latent representation that assists the further ECG pattern recovery, reducing the demand for radar-ECG pairs in the fine-tuning stage. The results of SSL are shown in Table 3.3 in terms of MSE and sparsity to illustrate the former and latter part (without  $\lambda_s$ ) in the loss function (3.10) for SSL training.

The experiment is repeated for different dataset scales with the ablation study on the use of sparse penalty, and the results indicate that both MSE and sparsity decrease with the reducing training data as shown in Table 3.3. Training with 100% or 80% dataset could achieve convergence and realize a successful SSR with similar MSE (0.91, 0.82) or (0.96, 0.85). However, the performance of SSR degrades heavily when further decreasing the training data without the constraint of sparse penalty, because the SSR results might fluctuate, as shown in Figure 3.10(a). In contrast, introducing the sparse penalty could suppress the fluctuation and force the deep learning model to focus only on the dominant peaks of the input radar signals, as

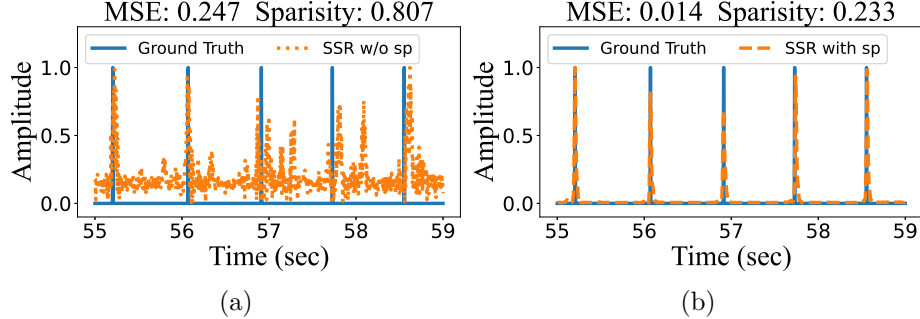


Figure 3.10: Results of SSR: (a) Failed SSR due to lack of data and sparse penalty; (b) Ideal SSR result with good MSE and sparsity.

shown in Figure 3.10(b). Therefore, the training with sparse penalty loss still achieves good results with an MSE of 0.92 and 0.98 by using 60% and 40% of the dataset, while the model cannot be well-trained without sparse penalty by using 40% dataset as shown in Table 3.3 and Figure 3.10(a).

### Evaluations of Fine-tuning Results

The fine-tuning is based on the model pre-trained by 100% dataset with or without sparse penalty, and the experiment is repeated for different percentages of labeled data (i.e., radar signal with ECG ground truth). In addition, the same deep-learning model will be trained in a supervised manner by using the same amount of labeled data as the reference for transfer-learning ECG recovery. At last, an overall improvement will be provided by calculating the percentage of improvement across all four metrics to provide straightforward evaluations for different methods, as shown in Table 3.4.

The fine-tuning with 100% labeled data provides very similar performance in morphological accuracy with the MSE and PCC around 0.0080 and 85.47%. It is worth noticing that the peak error and MDR are slightly improved, because the pre-text task SSR for pre-training is equivalent to identifying the peak position of the radar signal, and the learned representations can be seemly transferred to improve the accuracy of the recovered ECG R peaks, contributing to the overall improvement for transfer learning (3.66% and 1.75%).

Reducing 20% of labeled data causes a 10% overall degradation as shown in Table 3.4, and the decline of peak error and MDR is more than MSE and PCC. The reason is that ECG morphological patterns for different cardiac cycles are similar and can be well-learned from 80% labeled data with good MSE and PCC (0.0084 and 84.60%), while the location of each ECG piece is random and can be distorted by noises, requiring more training data for convergence.

The supervised training with 60% labeled data cannot ensure a good morphological and peak accuracy and the overall degradation is 23.37%, with the PCC drop below 80% as shown in Table 3.4. In contrast, the pre-trained model still provided good results with mild degradations of 8.71% and 12.68%. It is noticed that the effectiveness of sparse penalty in the SSL stage also affects the fine-tuning stage, because both peak error and MDR for transfer learning with spare penalty are better than those without sparse penalty, causing a large gap in the overall improvement compared with the previous training with 100% and 80% dataset.

Lastly, the deep learning model can barely learn from 40% labeled dataset and yield a bad morphological and peak accuracy for supervised learning. In addition, examples of the recovered ECG for transfer learning with or without sparse penalty are shown in Figure 3.11, and it is clear that the deep learning model struggles to learn both morphological and peak features from limited data if the pre-text task is not well-trained without sparse penalty, while Figure 3.11(b) shows the good recovery because the pre-trained model transfer the learned representations from radar inputs to ECG recovery.

### Summary of Transfer-learning-based ECG Recovery

Previous evaluations in terms of SSL and fine-tuning stages have illustrated the ability of the proposed RFcardi to learn from unlabeled data and transfer the knowledge to the ECG recovery task using limited radar-ECG pairs. The overall performance in Table 3.4 are plotted in Figure 3.12 for a straightforward comparison:

- The performance of supervised learning drops heavily and cannot ensure high-quality ECG recovery after reducing 40% labeled dataset.

Table 3.4: Performance of ECG Recovery using different percentages of labeled data

Methods	MSE ( $\times 10^{-2}$ ) ↓	PCC ↑	Peak Error (ms) ↓	MDR ↓	Overall ↑	MSE ( $\times 10^{-2}$ ) ↓	PCC ↑	Pea
<b>100% Labeled</b>								<b>80%</b>
Supervised	0.80	85.47%	7.61	6.85%	0.00%	0.84	84.60%	
TF w/o sp*	0.81	85.35%	8.46	5.51%	1.75%	0.82	86.36%	
TF with sp	0.80	85.51%	8.40	5.14%	3.66%	0.81	84.29%	
<b>60% Labeled</b>								<b>40%</b>
Supervised	0.93	79.91%	10.65	8.93%	-23.27%	0.98	75.89%	
TF w/o sp	0.85	83.74%	8.84	8.65%	-12.68%	0.97	76.56%	
TF with sp	0.86	84.92%	8.58	7.72%	-8.71%	0.93	78.72%	

\*TF for transfer learning and sp for sparse penalty

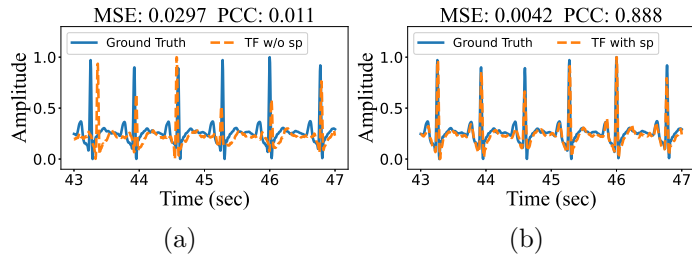


Figure 3.11: Results of transfer learning using limited labeled data: (a) Poor ECG recovery without proper morphological feature and peak location; (b) Good ECG recovery owing to the pre-trained model.

- Transfer learning could enhance the performance of ECG recovery for the cases with ample labeled training data, and the quality of the pre-trained model has a minor effect on the final result because the deep learning model could learn from numerous radar-ECG pairs.
- For the cases with limited labeled data (40%, 60%), the proposed RFcardi shows outstanding performance owing to the representations learned from unlabeled data. Furthermore, the quality of the pre-trained model does matter to alleviate the burden of deep learning model to learn both morphological ECG patterns

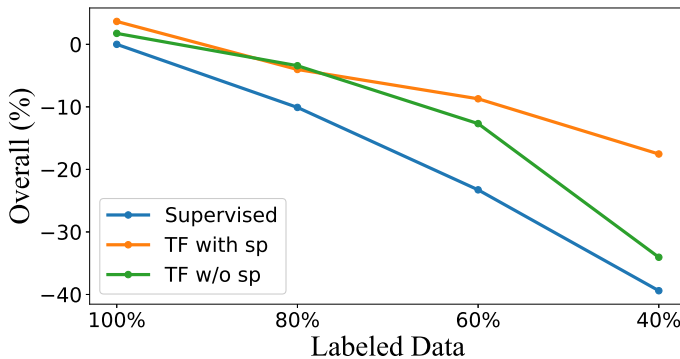


Figure 3.12: Overall performance of the radar-based ECG recovery.

and peak locations, as indicated by the increasing gap between orange and green lines in Figure 3.12.

## 3.6 Conclusions

This paper investigates the efficient collection of high-SNR radar signals with ample cardiac features for transfer-learning-based ECG recovery. Previous methods adopted signal accumulation or clustering to suppress the noises, while the rough localization based on FMCW radar cannot accurately reveal the chest region, requiring a time-consuming traverse among a 3D space for compensation. In this paper, a novel CFT algorithm is proposed to dynamically articulate the points with the best SNR and could track the cardiac location over time if the subjects change posture. In addition, a transfer learning framework RFcardi is designed with SSR as a pre-text task for pre-training to reduce the dependency on cumbersome ECG ground truth collection. The experiments performed in different scenarios prove the feasibility of the CFT-RFcardi framework in radar signal extraction and ECG recovery with limited labeled data, enabling a convenient deployment in new scenarios with limited data for future contactless wellness monitoring.

# **Chapter 4**

## **Chapter**

Another chapter.

# **Chapter 5**

## **Chapter**

Another chapter.

# **Chapter 6**

## **Chapter**

Another chapter.

# **Chapter 7**

## **Chapter**

Another chapter.

# Bibliography

- [1] World Health Organization, “Ageing and health,” 2024, <https://www.who.int/news-room/fact-sheets/detail/ageing-and-health>, Accessed: May. 7, 2025.
- [2] Y. Zhang, R. Yang, Y. Yue, E. G. Lim, and Z. Wang, “An overview of algorithms for contactless cardiac feature extraction from radar signals: Advances and challenges,” *IEEE Transactions on Instrumentation and Measurement*, Aug. 2023.
- [3] R. Guan, S. Yao, X. Zhu, K. L. Man, E. G. Lim, J. Smith, Y. Yue, and Y. Yue, “Achelous: A fast unified water-surface panoptic perception framework based on fusion of monocular camera and 4D mmWave radar,” in *2023 IEEE 26th International Conference on Intelligent Transportation Systems*. IEEE, Sep. 2023, pp. 182–188.
- [4] F. Wang, F. Zhang, C. Wu, B. Wang, and K. R. Liu, “Vimo: Multiperson vital sign monitoring using commodity millimeter-wave radio,” *IEEE Internet of Things Journal*, vol. 8, no. 3, pp. 1294–1307, 2020.
- [5] X. Chen, J. Cheng, R. Song, Y. Liu, R. Ward, and Z. J. Wang, “Video-based heart rate measurement: Recent advances and future prospects,” *IEEE Transactions on Instrumentation and Measurement*, vol. 68, no. 10, pp. 3600–3615, Nov. 2018.
- [6] D.-M. Chian, C.-K. Wen, C.-J. Wang, M.-H. Hsu, and F.-K. Wang, “Vital signs identification system with Doppler radars and thermal camera,” *IEEE Trans-*

- actions on Biomedical Circuits and Systems*, vol. 16, no. 1, pp. 153–167, Feb. 2022.
- [7] X. Xu, J. Yu, and Y. Chen, “Leveraging acoustic signals for fine-grained breathing monitoring in driving environments,” *IEEE Transactions on Mobile Computing*, vol. 21, no. 3, pp. 1018–1033, Mar. 2020.
- [8] W. Jia, H. Peng, N. Ruan, Z. Tang, and W. Zhao, “WiFind: Driver fatigue detection with fine-grained Wi-Fi signal features,” *IEEE Transactions on Big Data*, vol. 6, no. 2, pp. 269–282, Jun. 2020.
- [9] C. Feng, X. Jiang, M.-G. Jeong, H. Hong, C.-H. Fu, X. Yang, E. Wang, X. Zhu, and X. Liu, “Multitarget vital signs measurement with chest motion imaging based on MIMO radar,” *IEEE Transactions on Microwave Theory and Techniques*, vol. 69, no. 11, pp. 4735–4747, Nov. 2021.
- [10] I. Nirmal, A. Khamis, M. Hassan, W. Hu, and X. Zhu, “Deep learning for radio-based human sensing: Recent advances and future directions,” *IEEE Communications Surveys & Tutorials*, vol. 23, no. 2, pp. 995–1019, 2nd Quart. 2021.
- [11] W. Xia, Y. Li, and S. Dong, “Radar-based high-accuracy cardiac activity sensing,” *IEEE Transactions on Instrumentation and Measurement*, vol. 70, pp. 1–13, Jan. 2021.
- [12] Y. Wang, W. Wang, M. Zhou, A. Ren, and Z. Tian, “Remote monitoring of human vital signs based on 77-GHz mm-wave FMCW radar,” *Sensors*, vol. 20, no. 10, p. 2999, May 2020.
- [13] J. C. Lin, “Noninvasive microwave measurement of respiration,” *Proceedings of the IEEE*, vol. 63, no. 10, pp. 1530–1530, Oct. 1975.
- [14] S. M. Islam, O. Boric-Lubecke, V. M. Lubecke, A.-K. Moadi, and A. E. Fathy, “Contactless radar-based sensors: Recent advances in vital-signs monitoring of multiple subjects,” *IEEE Microwave Magazine*, vol. 23, no. 7, pp. 47–60, Jul. 2022.

- [15] U. Ha, S. Assana, and F. Adib, “Contactless seismocardiography via deep learning radars,” in *Proceedings of the 26th Annual International Conference on Mobile Computing and Networking (MobiCom)*, Apr. 2020, pp. 1–14.
- [16] A. B. Obadi, P. J. Soh, O. Aldayel, M. H. Al-Door, M. Mercuri, and D. Schreurs, “A survey on vital signs detection using radar techniques and processing with FPGA implementation,” *IEEE Circuits and Systems Magazine*, vol. 21, no. 1, pp. 41–74, Feb. 2021.
- [17] Q. Lv, L. Chen, K. An, J. Wang, H. Li, D. Ye, J. Huangfu, C. Li, and L. Ran, “Doppler vital signs detection in the presence of large-scale random body movements,” *IEEE Transactions on Microwave Theory and Techniques*, vol. 66, no. 9, pp. 4261–4270, Sep. 2018.
- [18] M. Nosrati and N. Tavassolian, “Accurate Doppler radar-based cardiopulmonary sensing using chest-wall acceleration,” *IEEE Journal of Electromagnetics, RF and Microwaves in Medicine and Biology*, vol. 3, no. 1, pp. 41–47, Mar. 2018.
- [19] M. Mercuri, I. R. Lorato, Y.-H. Liu, F. Wieringa, C. V. Hoof, and T. Torfs, “Vital-sign monitoring and spatial tracking of multiple people using a contactless radar-based sensor,” *Nature Electronics*, vol. 2, no. 6, pp. 252–262, Jun. 2019.
- [20] F. Cocconcelli, N. Mora, G. Matrella, and P. Ciampolini, “High-accuracy, unsupervised annotation of seismocardiogram traces for heart rate monitoring,” *IEEE Transactions on Instrumentation and Measurement*, vol. 69, no. 9, pp. 6372–6380, Jan. 2020.
- [21] L. M. Swift, M. W. Kay, C. M. Ripplinger, and N. G. Posnack, “Stop the beat to see the rhythm: excitation-contraction uncoupling in cardiac research,” *American Journal of Physiology-Heart and Circulatory Physiology*, vol. 321, no. 6, pp. H1005–H1013, Dec. 2021.
- [22] J. Chen, D. Zhang, Z. Wu, F. Zhou, Q. Sun, and Y. Chen, “Contactless electrocardiogram monitoring with millimeter wave radar,” *IEEE Transactions on Mobile Computing*, Dec. 2022.

- [23] J. Liu, J. Wang, Q. Gao, X. Li, M. Pan, and Y. Fang, “Diversity-enhanced robust device-free vital signs monitoring using mmWave signals,” *IEEE Transactions on Mobile Computing*, Jun. 2024.
- [24] Y. Li, C. Gu, and J. Mao, “A robust and accurate FMCW MIMO radar vital sign monitoring framework with 4-D cardiac beamformer and heart-rate trace carving technique,” *IEEE transactions on microwave theory and techniques*, Oct. 2024.
- [25] J. Xiong, H. Hong, L. Xiao, E. Wang, and X. Zhu, “Vital signs detection with difference beamforming and orthogonal projection filter based on SIMO-FMCW radar,” *IEEE Transactions on Microwave Theory and Techniques*, vol. 71, no. 1, pp. 83–92, 2022.
- [26] S. Dong, Y. Li, C. Gu, and J. Mao, “Robust cardiac timing detection technique with vectors analytic demodulation in Doppler cardiogram sensing,” *IEEE Transactions on Microwave Theory and Techniques*, Jan. 2024.
- [27] C. Ni, J. Pan, D. Du, X. Yang, C. Shi, S. Chen, D. Yang, and S. Liu, “Accurate heart rate measurement across various body postures using FMCW radar,” *IEEE Transactions on Instrumentation and Measurement*, vol. 73, pp. 1–13, Mar. 2024.
- [28] D. Zhang, X. Zhang, Y. Xie, F. Zhang, H. Yang, and D. Zhang, “From single-point to multi-point reflection modeling: Robust vital signs monitoring via mmWave sensing,” *IEEE Transactions on Mobile Computing*, Dec. 2024.
- [29] B. Li, W. Li, Y. He, W. Zhang, and H. Fu, “Radarnet: Non-contact ecg signal measurement based on fmcw radar,” *IEEE Transactions on Instrumentation and Measurement*, Oct. 2024.
- [30] H. Zhang, D. Zhang, R. Song, Z. Wu, J. Chen, L. Fang, Z. Lu, Y. Hu, H. Lin, and Y. Chen, “Umimo: Universal unsupervised learning for mmWave radar sensing with MIMO array synthesis,” *IEEE Transactions on Mobile Computing*, Feb, 2025.

- [31] J. Chen, D. Zhang, G. Zhang, H. Wang, Q. Sun, and Y. Chen, “Co-sense: Exploiting cooperative dark pixels in radio sensing for non-stationary target,” *IEEE Transactions on Mobile Computing*, Nov. 2024.
- [32] Z. Chen, T. Zheng, C. Cai, and J. Luo, “MoVi-Fi: Motion-robust vital signs waveform recovery via deep interpreted RF sensing,” in *Proceedings of the 27th Annual International Conference on Mobile Computing and Networking (MobiCom)*, Feb. 2021, pp. 392–405.
- [33] R. Orkand and R. Niedergerke, “Heart action potential: dependence on external calcium and sodium ions,” *Science*, vol. 146, no. 3648, pp. 1176–1177, Nov. 1964.
- [34] Y. Wu, H. Ni, C. Mao, and J. Han, “Contactless reconstruction of ECG and respiration signals with mmWave Radar based on RSSRnet,” *IEEE Sensors Journal*, Nov. 2023.
- [35] Z. Wang, B. Jin, S. Li, F. Zhang, and W. Zhang, “ECG-grained cardiac monitoring using UWB signals,” *Proceedings of the ACM on Interactive, Mobile, Wearable and Ubiquitous Technologies*, vol. 6, no. 4, pp. 1–25, Dec. 2023.
- [36] L. Zhao, R. Lyu, H. Lei, Q. Lin, A. Zhou, H. Ma, J. Wang, X. Meng, C. Shao, Y. Tang *et al.*, “AirECG: Contactless electrocardiogram for cardiac disease monitoring via mmWave sensing and cross-domain diffusion model,” *Proceedings of the ACM on Interactive, Mobile, Wearable and Ubiquitous Technologies*, vol. 8, no. 3, pp. 1–27, Sep. 2024.
- [37] Y. Wang, Z. Wang, J. A. Zhang, H. Zhang, and M. Xu, “Vital sign monitoring in dynamic environment via mmWave radar and camera fusion,” *IEEE Transactions on Mobile Computing*, Jun. 2023.
- [38] P. Wang, X. Ma, R. Zheng, L. Chen, X. Zhang, D. Zeghlache, and D. Zhang, “SlpRoF: Improving the temporal coverage and robustness of RF-based vital sign monitoring during sleep,” *IEEE Transactions on Mobile Computing*, Dec. 2023.

- [39] Y. Zhang, R. Guan, L. Li, R. Yang, Y. Yue, and E. G. Lim, “radarODE: An ODE-embedded deep learning model for contactless ECG reconstruction from millimeter-wave radar,” *IEEE Transactions on Mobile Computing*, Apr. 2025.
- [40] Y. Zhang, R. Yang, Y. Yue, and E. G. Lim, “radarODE-MTL: A multi-task learning framework with eccentric gradient alignment for robust radar-based ECG reconstruction,” *IEEE Transactions on Instrumentation and Measurement*, Apr. 2025.
- [41] Z. Chu, R. Yan, and S. Wang, “Vessel turnaround time prediction: A machine learning approach,” *Ocean & Coastal Management*, vol. 249, p. 107021, Mar. 2024.
- [42] Y. Zhang, S. Xiong, R. Yang, E. G. Lim, and Y. Yue, “Recover from horcrux: A spectrogram augmentation method for cardiac feature monitoring from radar signal components,” in *2025 47th Annual International Conference of the IEEE Engineering in Medicine and Biology Society (EMBC)*, Jul. 2025.
- [43] S. Yao, R. Guan, Z. Wu, Y. Ni, Z. Zhang, Z. Huang, X. Zhu, Y. Yue, E. G. Lim, H. Seo *et al.*, “Waterscenes: A multi-task 4D radar-camera fusion dataset and benchmark for autonomous driving on water surfaces,” *IEEE Transactions on Intelligent Transportation Systems*, Jul. 2023.
- [44] Y. Song, K. Zhang, T. Yan, T. Jin, Y. Dai, and T. Wang, “Dual-modal human pose reconstruction using 3D UWB radar images and point clouds,” *IEEE Transactions on Instrumentation and Measurement*, Mar. 2025.
- [45] C. Chen, J. Shi, L. Feng, H. Yi, C. Wang, and H. Chen, “A two-stage fault diagnosis method with rough and fine classifiers for phased array radar transceivers,” *IEEE Transactions on Instrumentation and Measurement*, Oct. 2024.
- [46] L. Zhao, R. Lyu, Q. Lin, A. Zhou, H. Zhang, H. Ma, J. Wang, C. Shao, and Y. Tang, “mmArrhythmia: Contactless arrhythmia detection via mmWave sensing,” *Proceedings of the ACM on Interactive, Mobile, Wearable and Ubiquitous Technologies*, vol. 8, no. 1, pp. 1–25, Mar. 2024.

- [47] M. Tang, P. Teckchandani, J. He, H. Guo, and E. Soltanaghai, “BSENSE: In-vehicle child detection and vital sign monitoring with a single mmWave radar and synthetic reflectors,” in *Proceedings of the 22nd ACM Conference on Embedded Networked Sensor Systems*, Nov. 2024, pp. 478–492.
- [48] Texas Instruments, “AWR1843 - Single-chip 76-GHz to 81-GHz automotive radar sensor integrating DSP, MCU and radar accelerator,” 2018, <https://www.ti.com/product/AWR1843>, Accessed: Mar. 8, 2025.
- [49] F. Wang, X. Zeng, C. Wu, B. Wang, and K. R. Liu, “mmHRV: Contactless heart rate variability monitoring using millimeter-wave radio,” *IEEE Internet of Things Journal*, vol. 8, no. 22, pp. 16 623–16 636, Nov. 2021.
- [50] X. Chen, R. Yang, Y. Xue, B. Song, and Z. Wang, “TFPred: Learning discriminative representations from unlabeled data for few-label rotating machinery fault diagnosis,” *Control Engineering Practice*, vol. 146, p. 105900, Feb. 2024.
- [51] J. Larson, M. Menickelly, and S. M. Wild, “Derivative-free optimization methods,” *Acta Numerica*, vol. 28, pp. 287–404, Jun. 2019.
- [52] F. He, T. Liu, and D. Tao, “Why Resnet works? residuals generalize,” *IEEE Transactions on Neural Networks and Learning Systems*, vol. 31, no. 12, pp. 5349–5362, Feb. 2020.
- [53] J. Dai, H. Qi, Y. Xiong, Y. Li, G. Zhang, H. Hu, and Y. Wei, “Deformable convolutional networks,” in *Proceedings of the IEEE International Conference on Computer Vision*, 2017, pp. 764–773.
- [54] P. O. Hoyer, “Non-negative matrix factorization with sparseness constraints,” *Journal of machine learning research*, vol. 5, no. Nov, pp. 1457–1469, Apr. 2004.
- [55] D. Makowski, T. Pham, Z. J. Lau, J. C. Brammer, F. Lespinasse, H. Pham, C. Schölzel, and S. A. Chen, “NeuroKit2: A Python toolbox for neurophysiological signal processing,” *Behavior Research Methods*, pp. 1–8, Feb. 2021.